

HEALTH AND MEDICINE

Ultrasound-triggered interfacial engineering-based microneedle for bacterial infection acne treatment

Yiming Xiang^{1,2,3}, Jiali Lu², Congyang Mao^{1,2,3}, Yizhou Zhu^{1,2,3}, Chaofeng Wang⁴, Jun Wu³, Xiangmei Liu^{2,4*}, Shuilin Wu^{5*}, Kenny Y. H. Kwan^{1,3}, Kenneth M. C. Cheung^{1,3}, Kelvin W. K. Yeung^{1,3*}

Acne is an inflammatory skin disease mainly caused by *Propionibacterium acnes*, which can cause local inflammatory reactions and develop into chronic inflammatory diseases in severe cases. To avoid the use of antibiotics and to effectively treat the site of acne, we report a sodium hyaluronate microneedle patch that mediates the transdermal delivery of ultrasound-responsive nanoparticles for the effective treatment of acne. The patch contains nanoparticles formed by zinc porphyrin-based metal-organic framework and zinc oxide (ZnTCPP@ZnO). We demonstrated activated oxygen-mediated killing of *P. acnes* with an antibacterial efficiency of 99.73% under 15 min of ultrasound irradiation, resulting in a decrease in levels of acne-related factors, including tumor necrosis factor- α , interleukins, and matrix metalloproteinases. The zinc ions up-regulated DNA replication-related genes, promoting the proliferation of fibroblasts and, consequently, skin repair. This research leads to a highly effective strategy for acne treatment through the interface engineering of ultrasound response.

INTRODUCTION

Acne is a skin disease that ranks as the most common skin disorder worldwide. Up to 80% of teenagers (and even adults) are affected by acne, which can leave permanent scarring and even affect teenager's psychological development (1–3). Anaerobic bacteria *Propionibacterium acnes* infection is the main cause of acne. Excessive lipid secretion of the skin causes blockage of pores, which leads to a hypoxic microenvironment of the skin, resulting in the proliferation of *P. acnes* in the skin microbiome and damaging normal tissues (4). *P. acnes* also stimulates skin cells to secrete proinflammatory factors, such as tumor necrosis factor- α (TNF- α), interleukins (ILs), and matrix metalloproteinases (MMPs) (2, 4).

Now, antibiotics are primarily used to fight skin bacterial infections. The most common way to treat acne is by taking antibiotics orally or using topical antibiotic creams (5–7). Because of the barrier effect of the skin, most drugs cannot be delivered through the skin to achieve a therapeutic effect (8–10). Furthermore, because acne occurs so frequently, the regular use of oral antibiotics may damage normal gut microbes and cause other side effects (11). Notably, *P. acnes* can secrete extracellular polysaccharides to form biofilms, making the bacteria resistant to general antibacterial agents and the inflammatory cells of the host (3). Therefore, the in situ use of effective antibacterial agents is the most effective way to treat acne.

In recent years, numerous researchers have studied microneedles (MNs) for drug loading (12–14). Because of their special morphology, MNs can easily penetrate the stratum corneum and enter the viable epidermis (15). Therefore, the principal benefit of using MNs is the promise of pain-free delivery and the delivery of active ingredients into the dermis to treat acne (16).

In view of the characteristics of *P. acnes* and the prevention of drug-resistant bacteria caused by drug abuse, we used MNs loaded with ultrasound response nanocomposite materials to achieve the treatment effect of acne infection (17). Ultrasound treatment can effectively penetrate the human skin and connective tissue to more than 5 cm under the skin (18). Ultrasound is also a safe inspection imaging technology that has been widely used in the biomedical field. Ultrasound responsive materials can produce reactive oxygen species (ROS) under ultrasound excitation, which can kill bacteria (19, 20). ROS can oxidize key cellular macromolecules through an energy transfer mechanism, thereby leading to bacterial killing, regardless of whether they are Gram-positive or Gram-negative bacteria (21–23). Metal-organic frameworks (MOFs) have been widely used in the field of biomedicine because of their special structure and photoresponsiveness (21). However, a single MOF has only a weak ultrasound response because of the rapid recombination of electron holes between its structures. The ultrasound response of MOFs can be effectively improved by introducing another semiconductor structure to form an interface effect between the two structures and to guide the transfer of electrons and the change of energy (24).

Here, the composite structure of zinc porphyrin-based MOF and zinc oxide (ZnTCPP@ZnO) was synthesized and loaded into sodium hyaluronate-synthesized MNs. After being pressed on the skin, the sodium hyaluronate MNs can dissolve into dermis and release the nanoparticles. The interface effect between the composite materials can greatly improve the sonocatalytic performance and effectively reduce the energy required for oxygen activation. Under ultrasound, oxygen changes from a ground state to an excited state by gaining more electrons through high interfacial charge transfer,

¹Department of Orthopaedics and Traumatology, Li Ka Shing Faculty of Medicine, The University of Hong Kong, Pokfulam, Hong Kong 999077, China. ²Biomedical Materials Engineering Research Center, Collaborative Innovation Center for Advanced Organic Chemical Materials Co-constructed by the Province and Ministry, Hubei University, Wuhan 430062, China. ³Shenzhen Key Laboratory for Innovative Technology in Orthopaedic Trauma, Department of Orthopaedics and Traumatology, The University of Hong Kong-Shenzhen Hospital, Shenzhen 518053, China. ⁴School of Life Science and Health Engineering, Hebei University of Technology, Tianjin 300401, China. ⁵School of Materials Science and Engineering, Peking University, Beijing 100871, China.

*Corresponding author. Email: liuxiangmei1978@163.com (X.L.); slwu@pku.edu.cn (S.W.); wkkyeung@hku.hk (K.W.K.Y.)

thus rapidly producing a large number of ROS that kill *P. acnes* and hence treat acne. Furthermore, zinc ions released from the nanomaterial up-regulate metallothioneins (*Mt*) 1 and *Mt*2 in skin fibroblasts. *Mts* can maintain zinc homeostasis in cells, and their up-regulation accelerates a variety of biochemical and molecular events of skin repair (25). Here, we demonstrate that the presence of zinc ions also up-regulates DNA replication-related genes replication factor C (*Rfc*) 3, *Rfc*4, DNA ligase I (*Lig*1), and mini-chromosome maintenance complex component 6 (*Mcm*6) in fibroblasts up-regulated, which further demonstrates the function of zinc ions in promoting fibroblast proliferation and supporting acne recovery (Fig. 1) (26–28).

RESULTS

Fabrication and characterization of the MN patch

Sodium hyaluronate was selected as the sole raw material for MN patch. Hyaluronate is a polysaccharide that naturally occurs in corneal skin and can absorb up to 1000 times its weight of water, retaining skin moisture for transdermal absorption. It has excellent biocompatibility and solubility and can be used with other materials to provide the ideal effect of promoting absorption (29). Here, a simple method was used to prepare MNs. In fig. S1A, sodium hyaluronate was dissolved in water, and the dissolved gel-like substance was applied all over the surface of the polydimethylsiloxane molds. The molds were vacuum-dried in an oven for 5 min. After the molded material was removed, the mold surface was coated again with sodium hyaluronate aqueous solution. The setup was dried at room temperature overnight, and the blank MN patch was removed from the mold. To load the MNs with ZnTCPP@ZnO, the prepared nanoparticles were mixed into the dissolved sodium hyaluronate, in the first step of patch fabrication, before repeating the subsequent steps described above. As shown in fig. S1 (B and C), the size of the blank MN patch was 10 mm by 10 mm, the number of MNs on the patch was $16 \times 16 = 256$, and the MNs were evenly

distributed on the patch. On the basis of the fluorescence microscopy results in Fig. 2A, the blank MNs fluoresced green under 490-nm blue light irradiation, with the height of individual MNs reported as 600 μm under high-magnification field of view. This height is high enough to penetrate the cuticle and epidermis ($\sim 100 \mu\text{m}$) of the skin to reach the dermis ($\sim 600 \mu\text{m}$) (30, 31). Regarding the ZnTCPP@ZnO MNs, as shown in fig. S1C, loading the ZnTCPP@ZnO nanoparticles caused a color darkening, and the patch emitted yellow fluorescence under blue light (Fig. 2B), given that the ZnTCPP@ZnO in the MNs would typically emit red fluorescence under blue light (fig. S1D). The field-emission scanning electron microscopy (FESEM) images (fig. S1, B1 and C1) of blank MNs and ZnTCPP@ZnO MNs evidenced that the dimension of the ZnTCPP@ZnO MNs remained unchanged after modification. The separation between the MNs is about 400 μm , and the tip diameter of a single MN is $\sim 50 \mu\text{m}$ only. It seems that the nanoparticles do not alter the MN morphology during the synthesis. Although this small size ensures sufficient pressure to penetrate the skin, sufficient mechanical strength is also important for MN penetration of the skin. In fig. S1E, the stress-strain curves of the MNs were obtained by measuring the displacement and force changes. The MN patch was pressed vertically at a speed of 0.1 mm/min at the test station with an initial force of 0.01 N. The curves of the two different samples showed a sudden drop in force, which was due to the bending of the MN, a phenomenon that persisted until the compression was complete (32). The strain distance between the beginning of the MN bending and the final complete compression is about 600 μm , consistent with the height of the MN. At the same time, although the strength of the MN was weakened after the addition of the nanoparticles, it was still higher than the minimum penetration strength of the skin (33). To verify the penetration effect and skin solubility of the MN patch, a penetration experiment was conducted using pig skin. In fig. S1F, the MN patch was pressed on the pig skin for 2 min and removed. The MNs on the surface of the patch were

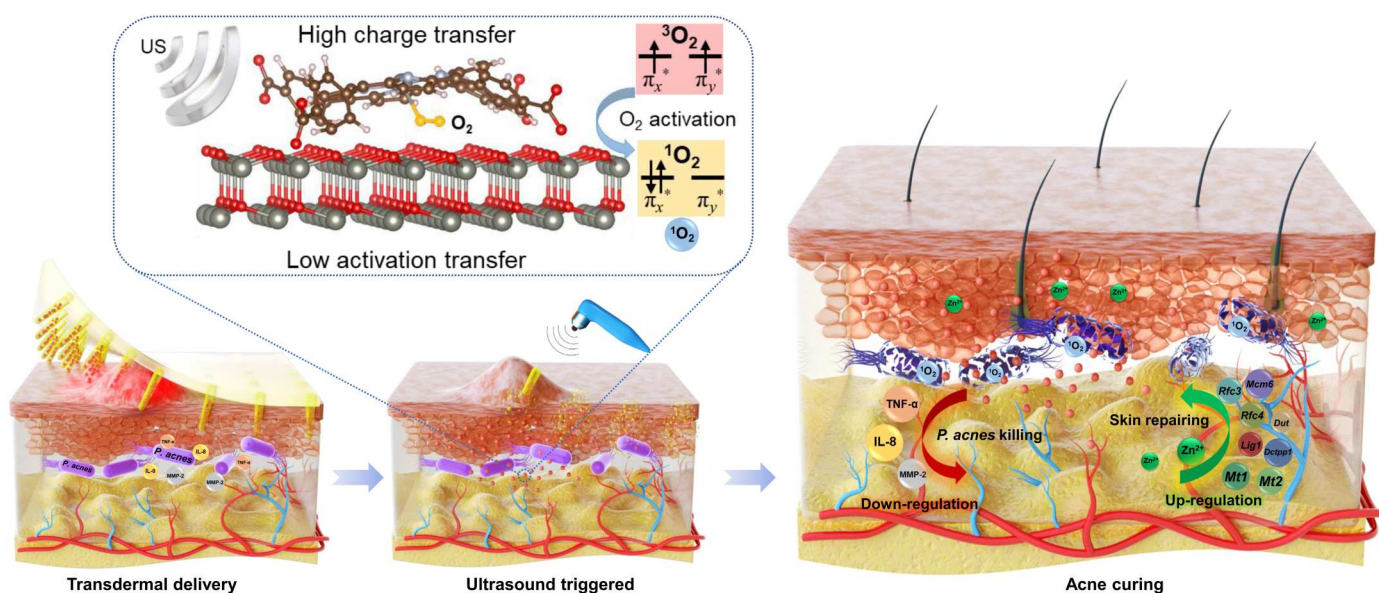


Fig. 1. Schematic diagram of MN therapy. Sonocatalytic mechanism and the treatment of acne through efficient sonodynamic ion therapy-based MN patch. US, ultrasound.

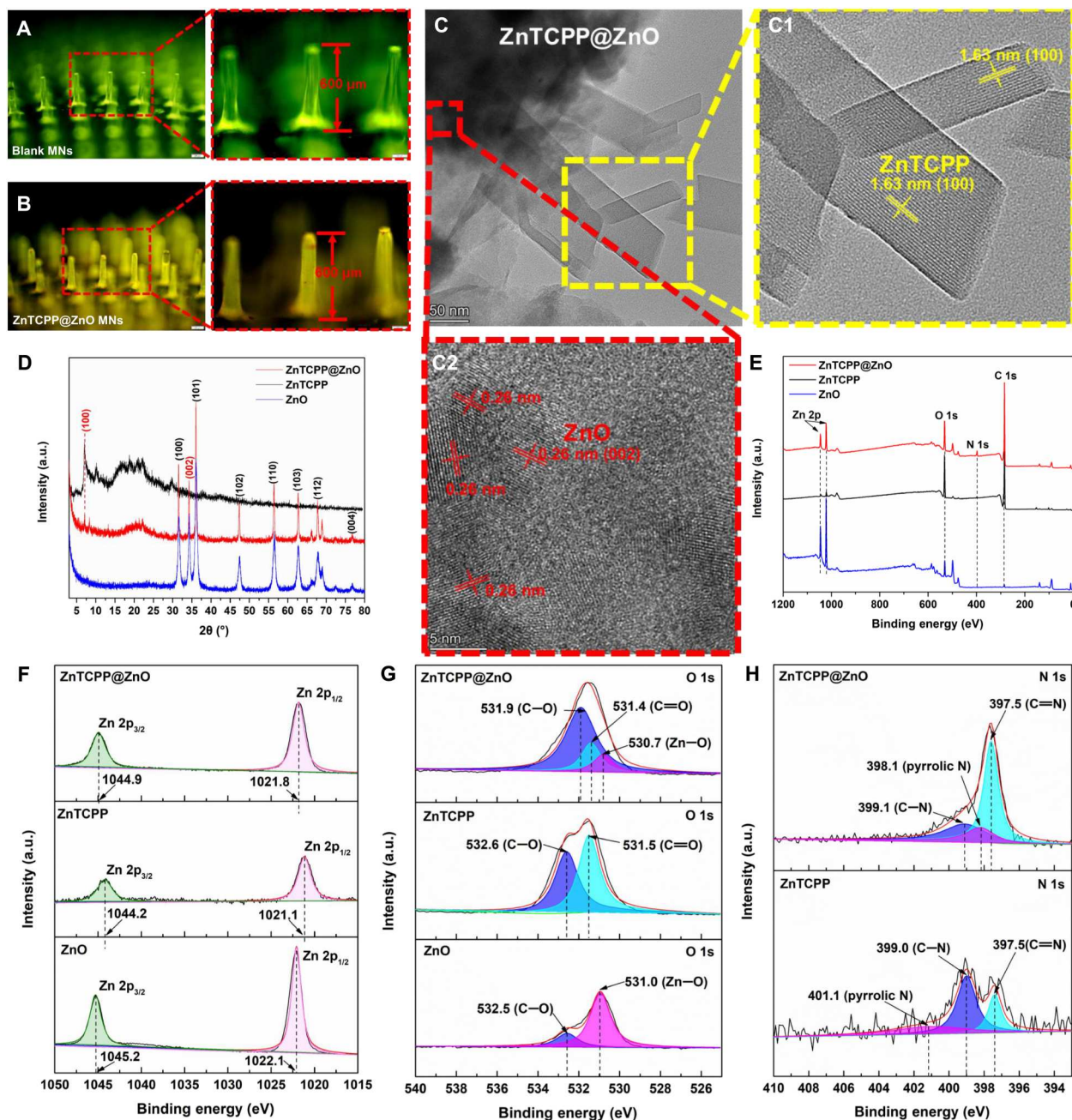


Fig. 2. Characterization of MN patch and ZnTCPP@ZnO nanoparticles. (A) Fluorescence images of blank MNs. (B) Fluorescence images of ZnTCPP@ZnO MNs. Scale bars, 100 μm (left) and 200 μm (right). (C) HRTEM image of ZnTCPP@ZnO. (C1) Magnified HRTEM image of ZnTCPP in ZnTCPP@ZnO. (C2) Magnified HRTEM image of ZnO in ZnTCPP@ZnO. (D) X-ray diffraction (XRD) patterns of ZnO, ZnTCPP, and ZnTCPP@ZnO. a.u., arbitrary units. (E) X-ray photoelectron spectroscopy (XPS) survey scan of ZnO, ZnTCPP, and ZnTCPP@ZnO. XPS high-resolution spectra of (F) Zn 2p peaks and (G) O 1s peaks obtained from ZnO, ZnTCPP, and ZnTCPP@ZnO. (H) XPS high-resolution spectra of N 1s peaks obtained from ZnTCPP and ZnTCPP@ZnO.

completely dissolved, leaving uniform pinholes on the surface of the pig skin. To verify the yield of the MN patch, the number of MNs on the patch was counted. The mold is designed with 256 MNs on one single patch, and the height of each MN measures at 600 μm . The results highlighted that the yield of the MNs and ZnTCPP@ZnO MN patches prepared by this method is 96.7% (table S1). In addition, we identified that the height of MNs can be maintained at 600

μm , when vacuum treatment is applied during fabrication. Together, these results show the successful fabrication of the MN patch and its loading with ZnTCPP@ZnO nanoparticles.

Characterization of ZnTCPP@ZnO nanoparticles

FESEM and high-resolution transmission electron microscopy (HRTEM) were used to observe the microstructure of

ZnTCPP@ZnO nanoparticles (Fig. 2C). The nanoparticles were mainly composed of regular four-sided rod-shaped ZnTCPP MOF and ZnO nanoparticles (fig. S2A), and the element mapping of HRTEM showed a uniform distribution of elements (C, O, N, and Zn) (fig. S2B). The HRTEM image in (Fig. 2C1) shows that the lattice fringe spacing of the rod-like structure is 1.63 nm, which is consistent with the computer-simulated crystal plane spacing of ZnTCPP (34). In the x-ray diffraction (XRD) patterns (Fig. 2D), the peak at 7.1° corresponds to the (100) crystal plane and appeared in both the black (pure ZnTCPP) and red (ZnTCPP@ZnO nanoparticles) curves, which is consistent with the literature (35). Furthermore, as shown in Fig. 2C2, the ZnO structure with 0.26-nm lattice fringes spacing can be seen, and the characteristic peaks of ZnO appear in both blue curve (pure ZnO) and red curve (ZnTCPP@ZnO nanoparticles) (Fig. 2D), which proves the presence of zinc oxide in ZnTCPP@ZnO nanoparticles, especially the peak located at 34.41° , which corresponds to the crystal plane (002) and consistent with (Fig. 2C2) (36, 37).

To further verify the structure of ZnTCPP@ZnO nanoparticles and the interaction between ZnO and ZnTCPP, x-ray photoelectron spectroscopy (XPS) tests were performed. Figure 2E shows C, O, and Zn in all three curves, and the carbon peak in ZnO may be due to the adsorption of CO_2 on the surface. The difference was that both the red and black curves had N, which came from the porphyrin ring in the ZnTCPP structure (38). To further confirmed the chemical bonding and interfacial interaction, the elemental peaks were analyzed and compared. As shown in Fig. 2F, the subpeaks at 1045.2 and 1022.1 eV were assigned to Zn $2p_{3/2}$ and Zn $2p_{1/2}$ in ZnO, and Zn $2p_{3/2}$ and Zn $2p_{1/2}$ in ZnTCPP were located at 1044.2 and 1021.1 eV (38, 39). In the composite structure of ZnTCPP@ZnO nanoparticles, the two characteristic peaks of Zn were Zn $2p_{3/2}$ (1044.9 eV) and Zn $2p_{1/2}$ (1021.8 eV), which were exactly located between pure ZnO and ZnTCPP. These changes in binding energy indicated that the zinc atom accepted the electron density of the porphyrins in the nanoparticles. Electrons of nitrogen in the porphyrin ring were transferred to an unoccupied metal orbital, forming a porphyrin-metal bond (40). When the density of the electron cloud increased, the shielding effect of the metal atom on the internal electrons also increased. Therefore, the binding energy of the inner shell of the electron was reduced (40, 41). In Fig. 2G, the O 1s region of the ZnO contained Zn—O (531.0 eV) and C—O (532.5 eV); the C—O group may also be caused by the adsorption of CO_2 on the surface. The O 1s region of the ZnTCPP contained C—O (532.6 eV) and C=O (531.5 eV), whereas the ZnTCPP@ZnO included C—O (531.9 eV), C=O (531.4 eV), and Zn=O (530.7 eV). Compared with ZnO, the Zn—O group in ZnTCPP@ZnO had a lower binding energy. The C—O group in ZnTCPP shifted to lower binding energy from 532.6 to 531.9 eV in ZnTCPP@ZnO (23). In Fig. 2H, the N 1s signals were located at the C—N (399.0 eV), C=N (397.5 eV), and pyrrolic N (401.1 eV) in ZnTCPP, whereas the pyrrolic N group in ZnTCPP@ZnO shifted to lower binding energy of 398.1 eV (24, 42). The peak shifts of Zn 2p, O 1s, and N 1s indicated the formation of a tight interface and electron interactions between ZnO and ZnTCPP (24, 43). In summary, these findings clarify the details of the structure and chemical bonds of ZnTCPP@ZnO nanoparticles.

Sonocatalytic activity of ZnTCPP@ZnO and theoretical calculations

Similar to the principle of photocatalysis, the efficiency of sonocatalysis is determined by the efficiency of electrons and hole separation and recombination under ultrasound irradiation (18, 44). Here, photoluminescence (PL) spectra were used to investigate the recombination efficiency of electron-hole pairs. In the PL results, the PL signal of ZnO was much higher than that of ZnTCPP and ZnTCPP@ZnO, which proves that the electron-hole pairs of ZnO recombine quickly (fig. S2C). The PL signal of ZnTCPP@ZnO was lower than that of ZnTCPP, indicating that the recombination of electron-hole pairs in the ZnTCPP@ZnO composite was inhibited (fig. S2D) (45, 46). Notably, in the ZnTCPP@ZnO curve, the peak at about 450 nm had an obvious red shift, indicating the electron state hybridization between ZnTCPP and ZnO (20, 47). The heterointerface between ZnTCPP and ZnO led to a longer lifetime of charge carriers crossing the interface, which reduced the recombination efficiency of electron-hole pairs and thus improved the sonocatalytic efficiency.

To further investigate the electron generation of materials under ultrasound irradiation, a sonoelectrochemical method was used to detect the generation of a sonocurrent. As shown in Fig. 3A, the ultrasound response current of ZnTCPP@ZnO was the most obvious in the continuous eight-cycle repeat of the on/off ultrasound. This result was consistent with the PL result, suggesting that inhibiting the recombination of electron-hole pairs can promote sonocurrent generation. Furthermore, the electron spin resonance (ESR) was used to detect ROS production in the materials during ultrasound irradiation. In Fig. 3B, the $^1\text{O}_2$ was tested by 2,2,6,6-tetramethylpiperidine, while the 5,5-dimethyl-1-pyrroline-*N*-oxide was used as the $\cdot\text{OH}$ probe (22, 48). The characteristic signal (1:1:1) of $^1\text{O}_2$ showed that, after 5 min of ultrasound irradiation, the signal intensity of ZnTCPP@ZnO was higher than that of ZnO and ZnTCPP (43, 48). The difference was that the characteristic signal (1:2:2:1) of $\cdot\text{OH}$ in ZnTCPP@ZnO was almost identical with that of ZnO and ZnTCPP (49). The $^1\text{O}_2$ detection of ZnTCPP@ZnO was tested by 1,3-diphenylisobenzofuran (DPBF); the yield of $^1\text{O}_2$ increased with the extension of ultrasound time (Fig. 3C). However, pure DPBF did not change with an increase in ultrasound time (fig. S3A).

To explore the mechanism of sonocatalytic, the Vienna Ab initio Simulation Package (VASP) was used to perform all the density functional theory (DFT) calculations (50, 51). Because the main species of ROS was $^1\text{O}_2$, the main purpose of calculation was to explore the oxygen activation and electron transfer of ZnTCPP@ZnO. The conversion of O_2 to $^1\text{O}_2$ was a process of energy transformation and electron transfer. The ground state of O_2 ($^3\text{O}_2$) had two unpaired electrons at the individual antibonding π orbital (π_x^* and π_y^*), while the excited state of O_2 ($^1\text{O}_2$) had paired electrons at the antibonding π orbital (π_x^*) (52, 53). Here, the electron transfer and the energy evolution produced by the material with ultrasound irradiation could help $^3\text{O}_2$ accomplished this transformation. Therefore, the site of oxygen adsorption on ZnTCPP@ZnO and the electrons transfer between two interfaces in ZnTCPP@ZnO were investigated by DFT calculations.

Before this, the structure of a single element of the ZnTCPP and ZnTCPP@ZnO was simulated in Fig. 3 (D and H). After oxygen adsorption, the results of differential charge density and Bader charge showed that there was an obvious charge transfer between the

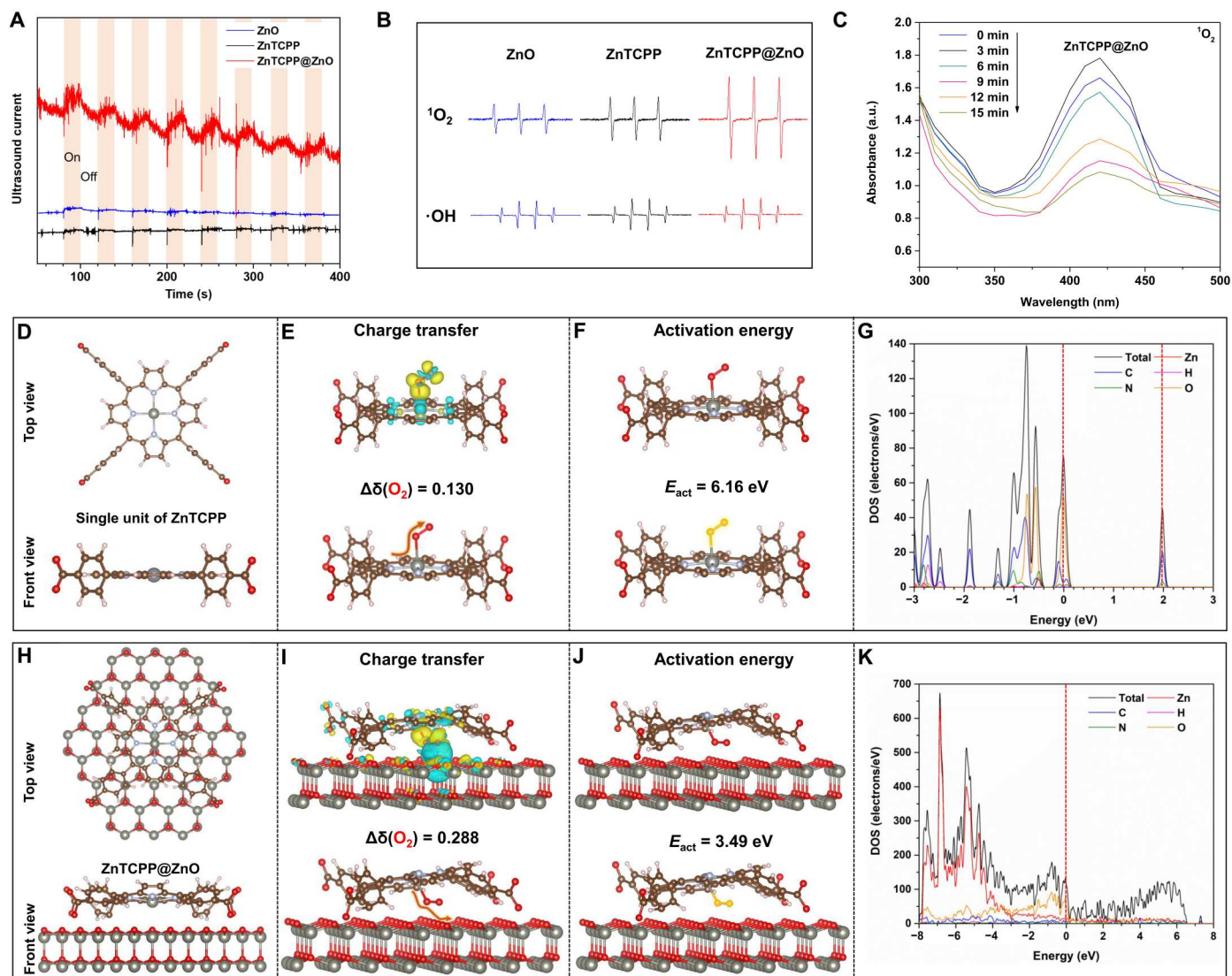


Fig. 3. Sonocatalytic activity and theoretical calculations of ZnTCPP@ZnO. (A) Ultrasound current responses of ZnO, ZnTCPP, and ZnTCPP@ZnO. (B) ESR measurements of $^1\text{O}_2$ and $\cdot\text{OH}$ of ZnO, ZnTCPP, and ZnTCPP@ZnO after ultrasound irradiation for 5 min. (C) $^1\text{O}_2$ detection of ZnTCPP@ZnO through DPBF. (D) ZnTCPP model structure from the top view and front view. (E) Charge density difference of ZnTCPP adsorbed O_2 and Bader charge. (F) O_2 activation energy of ZnTCPP. (G) Varied density of states of ZnTCPP. (H) ZnTCPP@ZnO model structure from the top view and front view. (I) Charge density difference of ZnTCPP@ZnO adsorbed O_2 and Bader charge. (J) O_2 activation energy of ZnTCPP@ZnO. (K) Varied density of states of ZnTCPP@ZnO.

oxygen adsorption site and O_2 (Fig. 3, E and I). Specifically, in the ZnTCPP model, O_2 can obtain electrons from ZnTCPP by forming Zn—O bonds, and the number of transferred electrons was calculated as 0.130 electron charge. By contrast, in the ZnTCPP@ZnO model, because of the interface effect between ZnO and ZnTCPP, electron transfer near O_2 increased, resulting in an increased number of electrons oxygen obtained; the calculated transferred electron charge was 0.288 electron charge. In addition to the enhanced amount of electron transfer in ZnTCPP@ZnO model, the calculation also showed that the oxygen activation process in ZnTCPP@ZnO model required less energy. As shown in Fig. 3F, according to the calculation of the ZnTCPP model, the activation energy required for O_2 to change from a ground state ($^3\text{O}_2$) to an excited state ($^1\text{O}_2$) was 6.16 eV. In the ZnTCPP@ZnO model, the

activation energy of O_2 was only 3.49 (Fig. 3J), much lower than that in the ZnTCPP model, proving that O_2 was more readily activated in the ZnTCPP@ZnO model (49).

Furthermore, the density of electronic states (DOS) calculation was conducted using the above two models. In Fig. 3 (G and K), the DOS of the ZnTCPP@ZnO indicated more hybridization at the Fermi level than ZnTCPP, which was also attributed to the interface effect between ZnO and ZnTCPP in the ZnTCPP@ZnO model (22). In summary, through the simulation calculation of electron transfer and energy evolution, the sonocatalytic mechanism of ZnTCPP@ZnO was elaborated in detail. Specifically, O_2 was adsorbed at the interface of ZnTCPP@ZnO due to the interface effect between ZnO and ZnTCPP in ZnTCPP@ZnO, and O_2 gains more electrons and energy. The energy required for O_2

activation in this structure was greatly reduced, which facilitated the transition of O₂ from the ground state to the excited state. These results indicated that the ZnTCPP@ZnO composite nanoparticles had superior sonocatalytic effects and can only produce one type of ROS (¹O₂) to provide support for antibacterial activities.

Antibacterial activity of the MN patch

P. acnes is the main bacterium that causes acne. To investigate the antibacterial effect of MNs against *P. acnes*, a spread plate method was used, as shown in fig. S4A. *P. acnes* with a concentration of 10⁵ colony-forming units (CFUs)/ml was chosen as the initial bacterial density. We observed only a slight change in the number of bacteria in the control group [phosphate-buffered saline (PBS)] with or without ultrasound. Similarly, for the blank MNs, ultrasound did not affect the growth of bacteria, and their numbers did not change too much. By contrast, after 15 min of ultrasound irradiation, the number of bacteria in ZnTCPP@ZnO MN group was reduced because of the substantial number of ROS produced by the ZnTCPP@ZnO nanoparticles in the MNs under ultrasound irradiation. Compared with the control group and blank MN group, the number of bacteria in ZnTCPP@ZnO MN group also decreased slightly without ultrasound irradiation, which may be due to the certain inhibitory effect of the zinc ions released from ZnTCPP@ZnO nanoparticles in MNs on bacteria (fig. S3B) (44, 54, 55).

To reflect the antibacterial effect more accurately, we counted the average CFU/ml of bacteria in each group. In the ultrasound group, the average CFU/ml of *P. acnes* in the control, blank MN, and ZnTCPP@ZnO MN group were 1.5×10^8 , 1.2×10^8 , and 8.8×10^7 , respectively. In the ultrasound+ group, the average CFUs/ml of *P. acnes* in the control, blank MN, and ZnTCPP@ZnO MN group were 1.5×10^8 , 1.1×10^8 , and 4.7×10^5 (Fig. 4A). According to the following formula: antibacterial efficiency (%) = (number of CFUs in the control group – number of CFUs in the experimental group)/(number of CFUs in the control group) × 100%, the antibacterial rate of ZnTCPP@ZnO MN group was calculated to be high as 99.73%.

The *P. acnes* morphology of different samples was observed by FESEM. As shown in Fig. 4B, except for the morphological folds (marked by red arrows) observed in the ZnTCPP@ZnO MNs under ultrasound irradiation, the bacteria in the other groups had complete cell morphology and regular rod-shaped shapes. In Fig. 4C, after ultrasound, the amount of protein leakage of *P. acnes* increased, and the amount of protein leakage in the ZnTCPP@ZnO MN group was the largest. This result was consistent with the previous spread plate results. The main reason for this difference was that, under the irradiation of ultrasound, ZnTCPP@ZnO produced a large number of ROS that destroyed the normal structure of the bacteria, leading to the contraction or even rupture of the bacterial cell membrane (44).

To further verify the antibacterial effect of MNs against drug-resistant bacteria, methicillin-resistant *Staphylococcus aureus* (MRSA) was selected to test the antibacterial effect of MNs. The results showed that the antibacterial trend of different groups against MRSA was consistent with the findings shown in Fig. 4A, and the ZnTCPP@ZnO MN group had the best antibacterial effect (fig. S4B). On the basis of the calculation of the CFU, we can conclude that the antibacterial efficiency of ZnTCPP@ZnO MN group reached 99.64% (fig. S5A). Similarly, the cell membrane

of MRSA was severely damaged by the ROS produced in the ZnTCPP@ZnO MN group under ultrasound irradiation (fig. S5, B and C), indicating that ROS produced by ZnTCPP@ZnO also had an excellent antibacterial effect on drug-resistant bacteria.

In vitro cytotoxicity studies and related mechanisms of cell regulation

The cell (NIH3T3, mouse embryonic fibroblast cell line) viability in different samples was evaluated using a 3-[4,5-dimethylthiazol-2-yl]-2,5-diphenyl tetrazolium bromide (MTT) assay and cell staining. In Fig. 4D, after 1 day of culture, in the control group and blank MN group, the large number of cells and the spread of the cellular matrix (green) around the nucleus (blue) confirmed that the cells were well spread and were highly active after 1 day. As for ZnTCPP@ZnO MN group, because ZnTCPP@ZnO had red fluorescence itself (fig. S1D), the red color showed up, but we could still observe many cells coexisting with the red powder coexistence, which indicates that dissolution of the MN into powder posed no cytotoxicity. We further acquired more quantitative results using the MTT results (Fig. 4E). After the first day, the MN group showed some effect on cell growth, but the number of cells increased gradually by the third and seventh days, indicating that the MNs themselves did not have an obvious toxic effect on cells. Especially in group ZnTCPP@ZnO MNs, the number of cells was higher from days 3 to 7 than in the other two groups. To verify the cellular toxicity of the MNs upon ultrasound stimulation, we supplemented an MTT assay under ultrasound irradiation for 15 min. The results shown in fig. S6 demonstrated that the transient ultrasound stimulation does not alter the cell viability as compared with the control, implying that the ROS induced by ZnTCPP@ZnO microstructures will unlikely cause the issue of cytotoxicity. Thus, ZnTCPP@ZnO MN group had a certain promoting effect on cell proliferation.

To further confirm the skin repair effect of the ZnTCPP@ZnO MNs on skin infection, a cell migration assay was also performed. In Fig. 4F, the amount of cell migration was higher in ZnTCPP@ZnO MN group, twice as much as in the other two groups (Fig. 4E). This phenomenon may be due to the regulation of cells by zinc ions released from the ZnTCPP@ZnO MN group. To ascertain that ZnTCPP@ZnO could promote cell proliferation, we conducted transcriptome sequencing on cells cotreated with different materials. As shown in Fig. 5A, based on the expression of genes in different groups, the correlation behavior analysis between the groups tested whether the variation between biological repeats met the expectations of the experimental design. The left and top sides represent the clustering situation of each group. Squares of different colors represent the correlation levels of the two groups. The larger the value, the greater the correlation between the two groups, and the more similar it was. The correlation between the control group and the blank MN group was good. However, the gene expression of the ZnTCPP@ZnO MN group was different from that of the other two groups. As shown in Fig. 5B, compared with the control group, the ZnTCPP@ZnO MN group had 4948 differentially expressed genes (2920 down-regulated and 2028 up-regulated). In Fig. 5C, compared with the blank MN group, the ZnTCPP@ZnO MN group still had 3994 differentially expressed genes (2547 down-regulated and 1447 up-regulated). In Fig. 5D, between the control group and the blank MN group, there were only 627 differentially expressed genes (476 down-regulated and

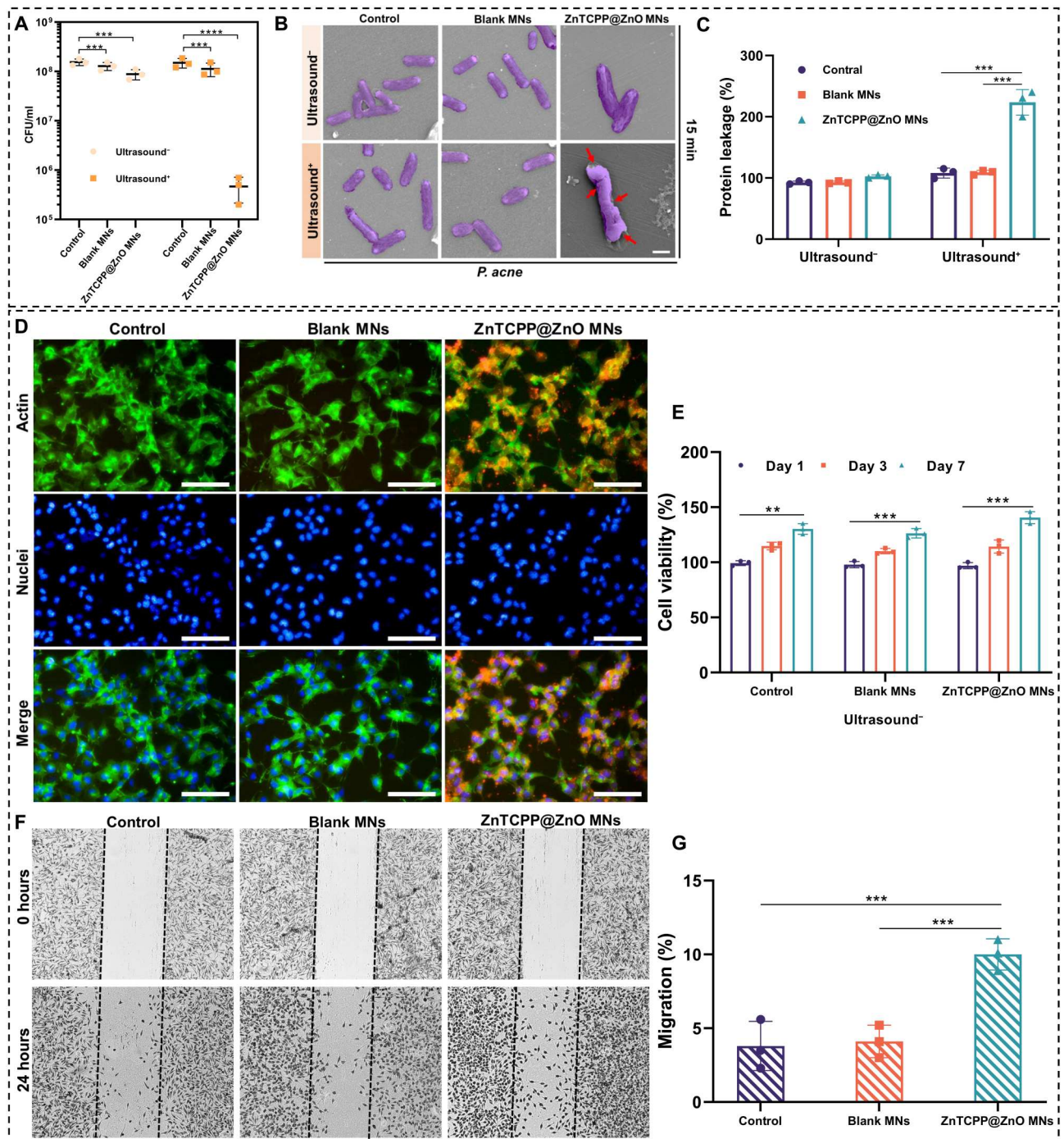


Fig. 4. Antibacterial activity and cytocompatibility of the MNs. (A) Number of *P. acne* colonies after treatments with different samples. (B) SEM images of *P. acne* colonies after treatments with different samples. Scale bar, 1 μm . (C) Protein leakage concentration for *P. acne*. (D) Fluorescent images of NIH3T3 cultured with various samples for 1 day. Actin is stained with fluorescein isothiocyanate (green), and nuclei is stained with 4',6'-diamidino-2-phenylindole (blue) at a cell density of 4×10^5 cells/ml. Scale bar, 100 μm . (E) MTT assay of cell viability. Cells were cultured on different samples for 1, 3, and 7 days. (F) Scratch assay images of NIH3T3 cultured with various samples for 1 day. (G) Cell migration quantification of NIH3T3. $n = 3$ independent experiments per group. Statistical differences were analyzed by one-way analysis of variance (ANOVA) and post hoc Tukey's test (** $p < 0.01$, *** $p < 0.001$, and **** $p < 0.001$).

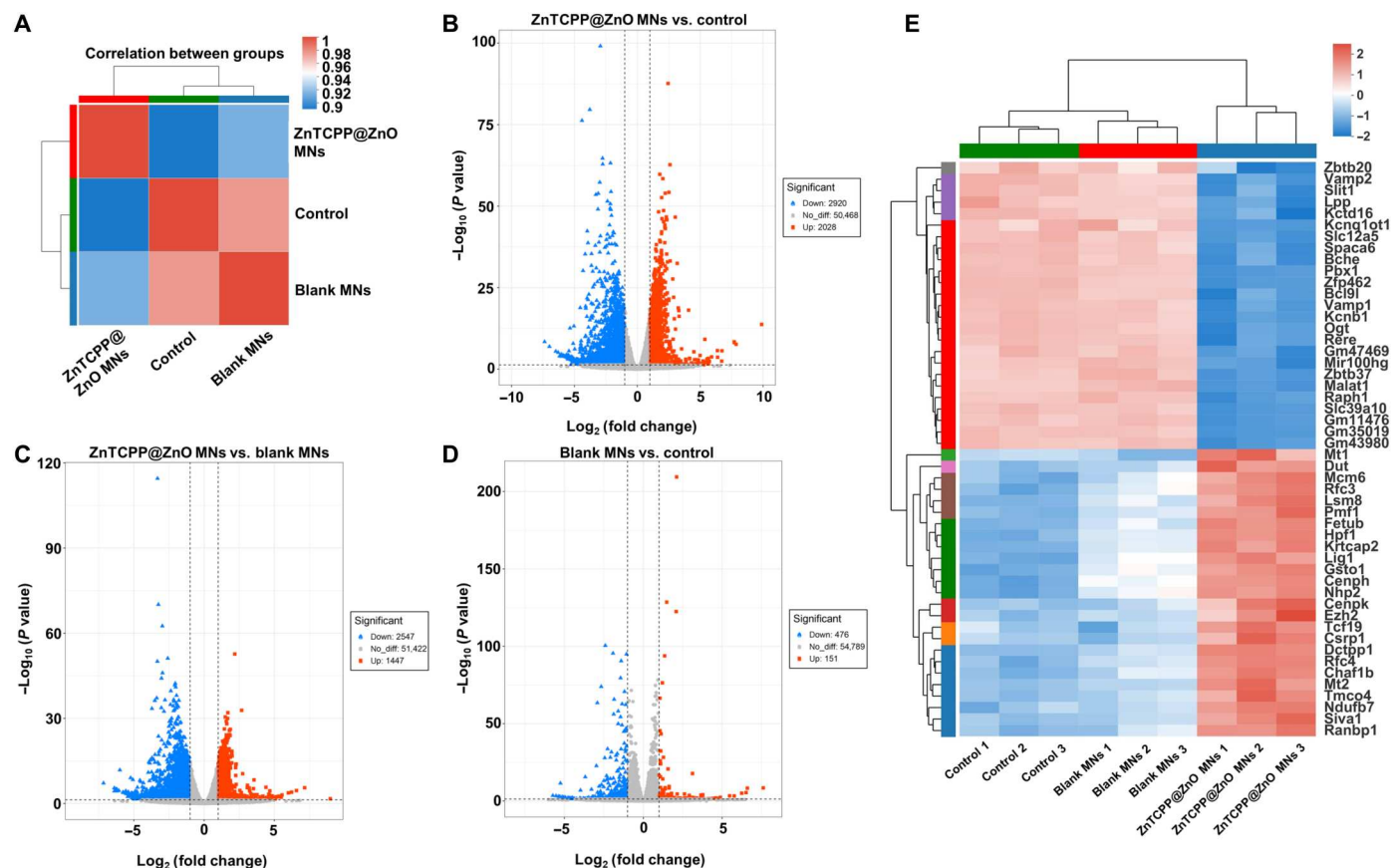


Fig. 5. Analysis of gene expression correlation and differential gene expression between different samples. (A) Correlation heatmap analysis between different groups. Each group has three parallel samples. (B to D) Volcano plots of differentially expressed genes between different groups. The red dots represent genes that are up-regulated, the blue dots represent genes that are down-regulated, and the gray dots represent genes that are not different. (E) Clustering heatmaps of the top 25 up-regulated and 25 down-regulated differential genes. Red represents high expression of the gene in the sample, and blue represents low expression.

151 up-regulated). These results suggest that the ZnTCPP@ZnO component in ZnTCPP@ZnO MN group was the main factor driving gene differential expression.

To further analyze the function of the differential genes, we extracted the top 50 differentially expressed genes (25 down-regulated and 25 up-regulated from Fig. 5, B and C). The heatmap in Fig. 4E showed that these 50 target genes were consistently up-regulated or down-regulated in all the samples from the ZnTCPP@ZnO MN group compared to the other two groups.

Gene Ontology (GO) and Kyoto Encyclopedia of Genes and Genomes (KEGG) enrichment analyses were performed to study the function of these 50 target genes. In Fig. 6 (A and B), the horizontal axis represents the rich factor—the larger the rich factor, the greater the degree of enrichment. The size of the bubble represents the number of genes, and the color of the bubble corresponds to different P_{adjust} (adjusted P value) ranges. In the GO enrichment analysis, the target genes were mainly enriched in DNA replication, cellular zinc ion homeostasis, and pyrimidine deoxyribonucleotide binding. In KEGG enrichment analysis, target genes were mainly enriched in DNA replication, mismatch repair, mineral absorption, and the pyrimidine metabolism pathway.

To identify the genes that regulate these functions more intuitively, an enrichment chord diagram was constructed for analysis,

as shown in Fig. 5 (C and D). The main functions of the target genes in the two differential enrichment analyses focused on DNA replication and metal ion homeostasis. The target genes were *Rfc4*, *Rfc3*, *Lig1*, *Mcm6*, *Mt1*, *Mt2*, *Dut*, and *Dctcp1*. The genes involved in DNA replication—*Rfc4*, *Rfc3*, *Lig1*, and *Mcm6*—were up-regulated in the ZnTCPP@ZnO MN group (26–28). *Dut* and *Dctcp1* genes, which were highly expressed in the proliferation cells, were also up-regulated in the ZnTCPP@ZnO MN group (56, 57). These were consistent with MTT data, proving that cell proliferation in ZnTCPP@ZnO MN group was faster than that in the other two groups. To explore the mutual use of proteins corresponding to these genes, these genes were submitted to the STRING database to construct a protein-protein interaction (PPI) network, as shown in Fig. 6E. The network revealed that the proteins of differential genes associated with DNA replication and cell proliferation were highly correlated, especially *Rfc4*. Furthermore, the expression levels of *Mt1* and *Mt2* genes, which are involved in the process of intracellular metal ion adsorption and mitosis promotion in cell behavior, were highly related to their PPI-suggested involvement with zinc ions (25, 44). To verify the expression of target genes in different groups, fibroblasts cocultured with different groups were subjected to RNA extraction and quantitative real-time polymerase chain reaction (qRT-PCR) testing, as shown in Fig. 6F. All eight

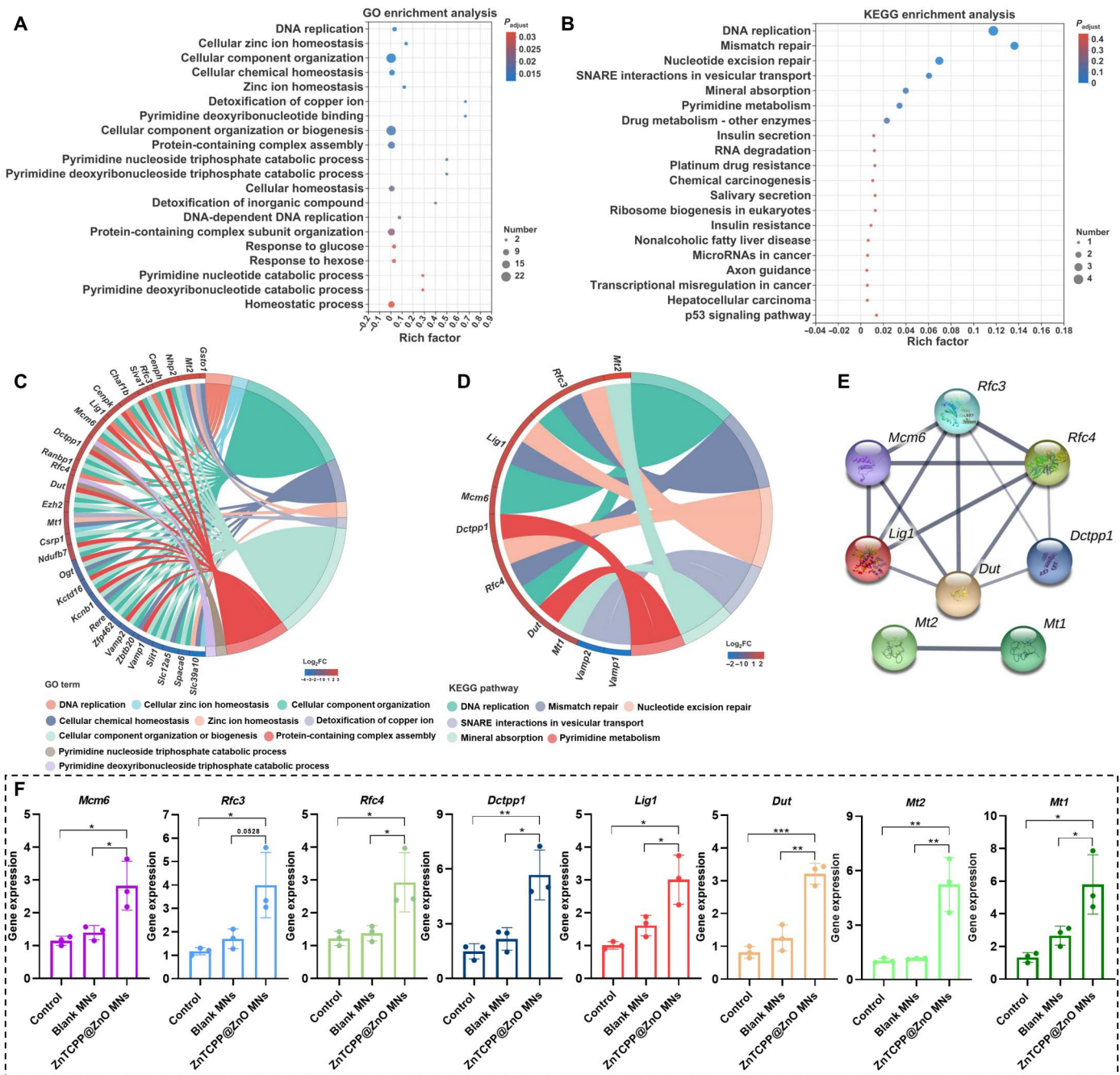


Fig. 6. Functional analysis of target genes and qPCR in different samples. (A) GO enrichment analysis of biological processes of the top 25 up-regulated and 25 down-regulated differential genes. (B) KEGG pathway enrichment analysis of the top 25 up-regulated and 25 down-regulated differential genes. SNARE, soluble N-ethylmaleimide-sensitive factor attachment protein receptor. (C) GO term enrichment of chord diagram. (D) KEGG pathway enrichment of chord diagram. (E) Protein-protein interaction (PPI) network analysis on target genes. The more connected lines, the higher the interaction correlation. (F) Expression of target genes in different treated groups. $n = 3$ independent experiments per group. Statistical differences were analyzed by one-way ANOVA and post hoc Tukey's test ($*P < 0.05$, $**P < 0.01$, and $***P < 0.001$).

genes were more highly expressed in the MN group with ZnTCPP@ZnO nanoparticles.

We then analyzed the secretion of fibroblast-related cytokines by enzyme-linked immunosorbent assay (ELISA). The results are shown in fig. S7, which is in good agreement with the above results. Stimulated by the material, the cells secreted more cytokines

related to cell proliferation in ZnTCPP@ZnO MNs group. Combined with the previous results, these findings indicate that zinc ions released by ZnTCPP@ZnO promoted the proliferation of fibroblasts, which would support skin repair.

In vivo anti-acne performance of the MN patch

Before we proceeded to the animal study, a hemolysis test on MNs had been conducted. The results suggested that both of the blank MNs and ZnTCPP@ZnO MNs do not induce hemolysis (fig. S8). To evaluate the effect of a MN patch on *P. acnes* infection, we created an acne model by intradermal injection of *P. acnes* into the back of Balb/c mice. All acne model mice were then randomly divided into six groups ($n = 5$). At day 0, different groups of mice were treated with the different materials, and acne was observed and analyzed at 1, 3, and 7 days (Fig. 7A). Group 1 (G1) was the control

group, with no treatment. G2 was treated with an acne drug, Mentholatum Acnes Point Clear, three times on day 0. G3 was treated with blank MNs by pressing the blank MN patch on the acne for 3 min, after which the needles dissolved in the dermis, and the patch was removed before a 10-min ultrasound irradiation. G4 was treated with ZnTCPP@ZnO patch (without needles on the patch) by pressing the patch on the acne with 10-min ultrasound irradiation. Note that the purpose of setting group G4 was to verify whether the patch alone can release material into the acne lesions under the ultrasound without needle. G5 was treated with ZnTCPP@ZnO MNs by

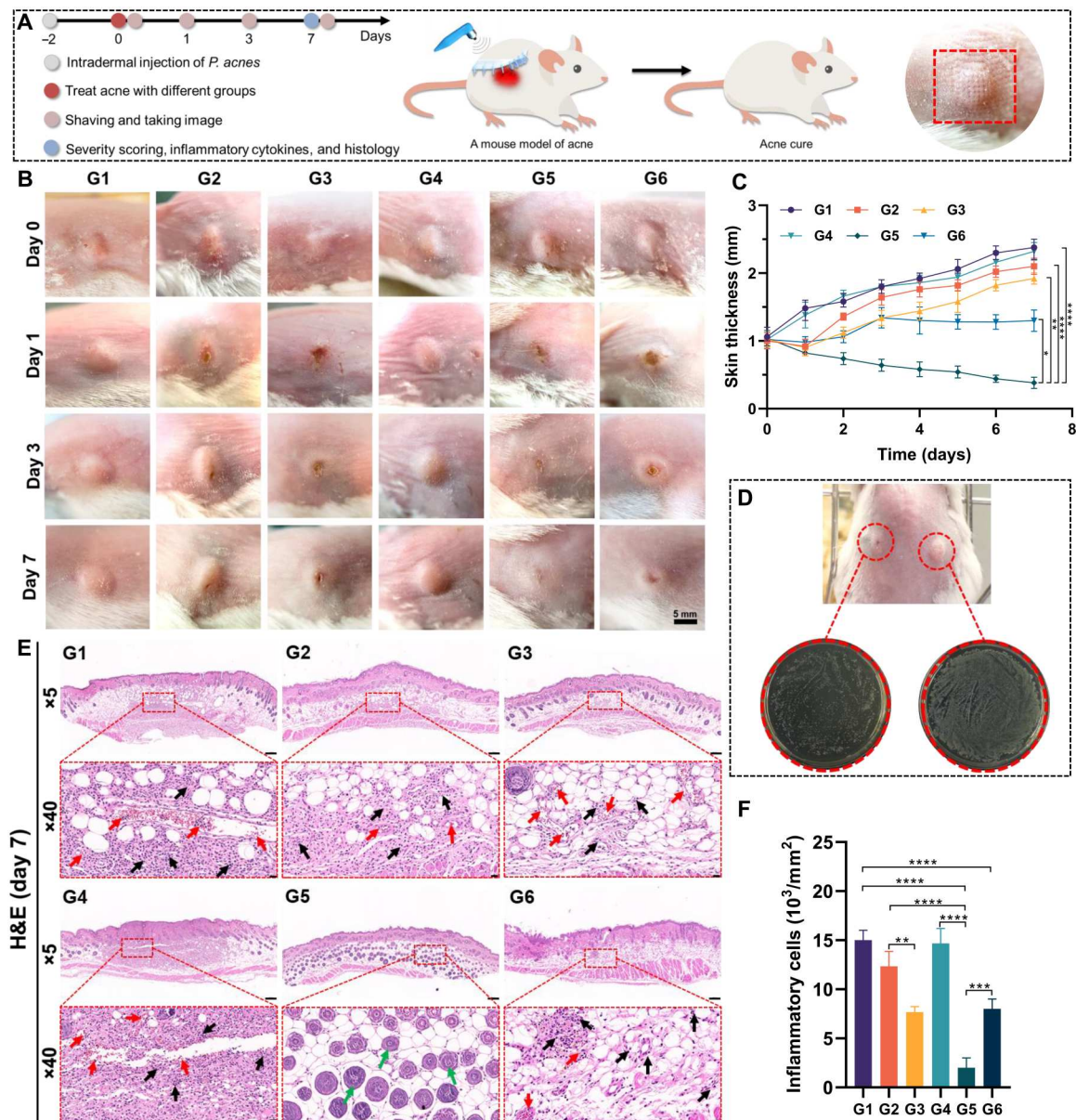


Fig. 7. Mitigation of acne via different MN patch. (A) Schematic illustration of the MN patch for the treatment of acne. (B) Photographs of mice treated with various treatments. Scale bar, 5 mm. (C) Quantitative analysis of thickness of skin from mice in each group. (D) Two acne models on the back of the same mouse. (The acne on the left was the same treatment as that in G5, while the acne on the right was untreated.) (E) Hematoxylin and eosin (H&E) staining of the skin tissue sections from the mice after the different treatments (magnification, $\times 5$ and $\times 40$; scale bars, 200 and 20 μm , respectively). (F) Quantitative analysis of infiltrated inflammation cells in each group. $n = 3$ independent experiments per group. Statistical differences were analyzed by one-way ANOVA and post hoc Tukey's test ($*P < 0.05$, $*P < 0.01$, $***P < 0.001$, and $****P < 0.0001$).

pressing the ZnTCPP@ZnO MN patch on the acne for 3 min, after the needles were dissolved in the dermis, the patch was removed and followed by 10-min ultrasound irradiation. G6 received the same treatment as G5 but without ultrasound. Microscopic pores were observed on the skin surface of mouse model with acne infection after MN patch was applied (Fig. 7A). When examined under SEM, almost all the MNs disappeared after the application (fig. S9, A and B). In addition, the result of hematoxylin and eosin (H&E) staining suggested that the MNs were completely dissolved in the epidermal layer of mouse model after 1 day of application (fig. S9C).

As shown in Fig. 7B, at day 0 (2 days after intradermal injection of *P. acnes*), acne approximately 1 mm thick formed at the injection site due to bacterial infection and proliferation, demonstrating the successful construction of the *P. acnes* infection acne model (58). After the MNs were pressed on the surface of acne, pinholes with uniform distribution and size could be seen on the surface, which proved that the MNs could effectively penetrate the surface of acne (Fig. 7A). In G1, the size of the untreated acne increased over time due to infection. The same trend also appeared in G4, indicating that, in the absence of needles on the patch, a single patch could not effectively deliver nanoparticles to the infected site. Despite ultrasound irradiation, the infected site was still not effectively treated due to dermis blocking. To ensure consistency in G2, which used the acne drug, the drug was applied three times on day 0. We observed a certain degree of inhibition on day 1 with drug use, but, on days 3 and 7, the acne returned. This may be due to the fact that it was difficult to penetrate the dermis to kill bacteria effectively with a single-day drug treatment.

As for G3 blank MNs, because they were not loaded ZnTCPP@ZnO nanoparticles, although the needles dissolved in the dermis, they did not have sufficient antibacterial effect under ultrasound irradiation; only some physical piercing effect was observed on the acne. A similar piercing effect also appeared in G6. Although G6 was treated with loaded ZnTCPP@ZnO nanoparticles, ultrasound was not used, resulting in no ROS generation, and the inhibiting effect on acne only came from zinc ions released by the nanoparticles (fig. S3B). Therefore, the effect of G6 was slightly better than that of G3 (Fig. 7C). By contrast, the treatment effect of G5 was better than that of the other groups, and acne was almost completely treated by day 7 after treatment. This was because the MNs help the ZnTCPP@ZnO nanoparticles enter the infected dermis area, and, when stimulated by ultrasound, the nanoparticles in the dermis release a large number of ROS, killing *P. acnes*, and the zinc ions helped the skin repair, allowing acne to be effectively treated.

To further demonstrate the therapeutic effect of G5, two acne models were created on the back of the same mouse. The acne on the left was the same treatment as that in G5, while the acne on the right was untreated. The size of the treated acne after 7 days was smaller than that of the untreated acne on the right (Fig. 7D). To verify the bacterial inhibition effect, skin tissue from two acne sites was taken out and ground up, and the number of bacteria inside the acne was observed using the spread plate method (Fig. 7D). The number of bacteria in treated acne was much lower than in untreated acne. To quantify the treatment effect of acne, the thickness of acne was measured during the treatment (Fig. 7C), revealing a change in acne thickness that was consistent with the treatment effects observed in Fig. 7B.

To further evaluate the effect of MNs on acne, mice were euthanized on day 7, and skin tissue from the acne site was excised for histological and immunohistochemical analysis. H&E staining (5 \times ; Fig. 7E) revealed that the thickness of the skin section in G5 was thinner than in the other groups, which was consistent with the result presented in Fig. 7C. As shown in the $\times 40$ H&E staining images, the skin tissue in G1 and G4 had an abundance of infiltrated inflammatory cells (black arrows). Red blood cells (RBCs) that flowed out from ruptured vessels were observed at some sites (red arrows). Similarly, although the number of inflammatory cells in G2, G3, and G6 was small, a certain degree of infiltrated inflammatory cells was observed. By contrast, a clear and intact reticular layer of dermis and hair follicle structures can be observed in G5's skin tissue due to its excellent anti-infection properties. Quantitative analysis also proved that G5 had the lowest number of inflammatory cells and the best therapeutic effect (Fig. 7F).

P. acnes is an anaerobic Gram-positive bacterium. Its overproliferation encourages the synthesis of lipid droplets and triacylglycerol by mouse skin sebum cells, causing sebum accumulation to clog hair follicles, further causing hypoxia in the skin and promoting bacterial growth (2). *P. acnes* induces and exacerbates inflammation, inducing keratinocytes to produce IL-8, TNF- α , and MMP-2 (59). Immunohistochemical results showed the expression of these three proteins in the acne area in detail. In Fig. 8, except for G5, cells with intense staining for the IL-8 protein can be observed in other groups. The results of the optical density analysis intuitively showed that the expression of inflammatory factors in G5 was the lowest. The same trend can be observed in the results of TNF- α and MMP-2. It was proved again that the excellent bacterial effect of G5 reduced the expression of these inflammatory factors and proteins and had the best therapeutic effect.

To further confirm the biosafety of the ZnTCPP@ZnO MNs, the blood from the mice on day 7 was extracted for routine blood analysis. As shown in Fig. 8D, all data were within the corresponding normal scope (marked by dotted line), including white blood cell count, monocyte, granulocyte, platelet count, lymphocyte, RBC count, hematocrit, and hemoglobin. In addition, the corresponding histological analyses of the major organs (heart, liver, spleen, lung, and kidney) based on H&E staining (fig. S10) showed no signs of organ damage. Together, these results further confirmed that the ZnTCPP@ZnO MNs had excellent biosafety and immense potential for clinical treatment for bacterial infection acne.

DISCUSSION

The conventional acne treatments mainly include the epidermal administration of antibiotics or the physical puncture to drain out the pus from lesion. However, repeated applications of antibiotics may reduce the sensitivity of bacteria to drugs (2, 6, 9). In addition, the treatment efficiency can be potentially reduced due to the permeability of epidermal barrier. Physical and psychological shock to the patients had been documented, when long-term and repeated onset of acne infection happened. Hence, oral medication and psychological intervention are advised to those severe cases (59). We believe that the treatment via ROS-enabled MNs, regarding as a minimal invasive and transdermal approach, can effectively relieve the acne infection (8). MNs serving as the delivery vehicle of antibiotics or nonantibiotic substances to address bacterial infection have been studied (4, 9, 15). In the current design, we introduce ultrasound-

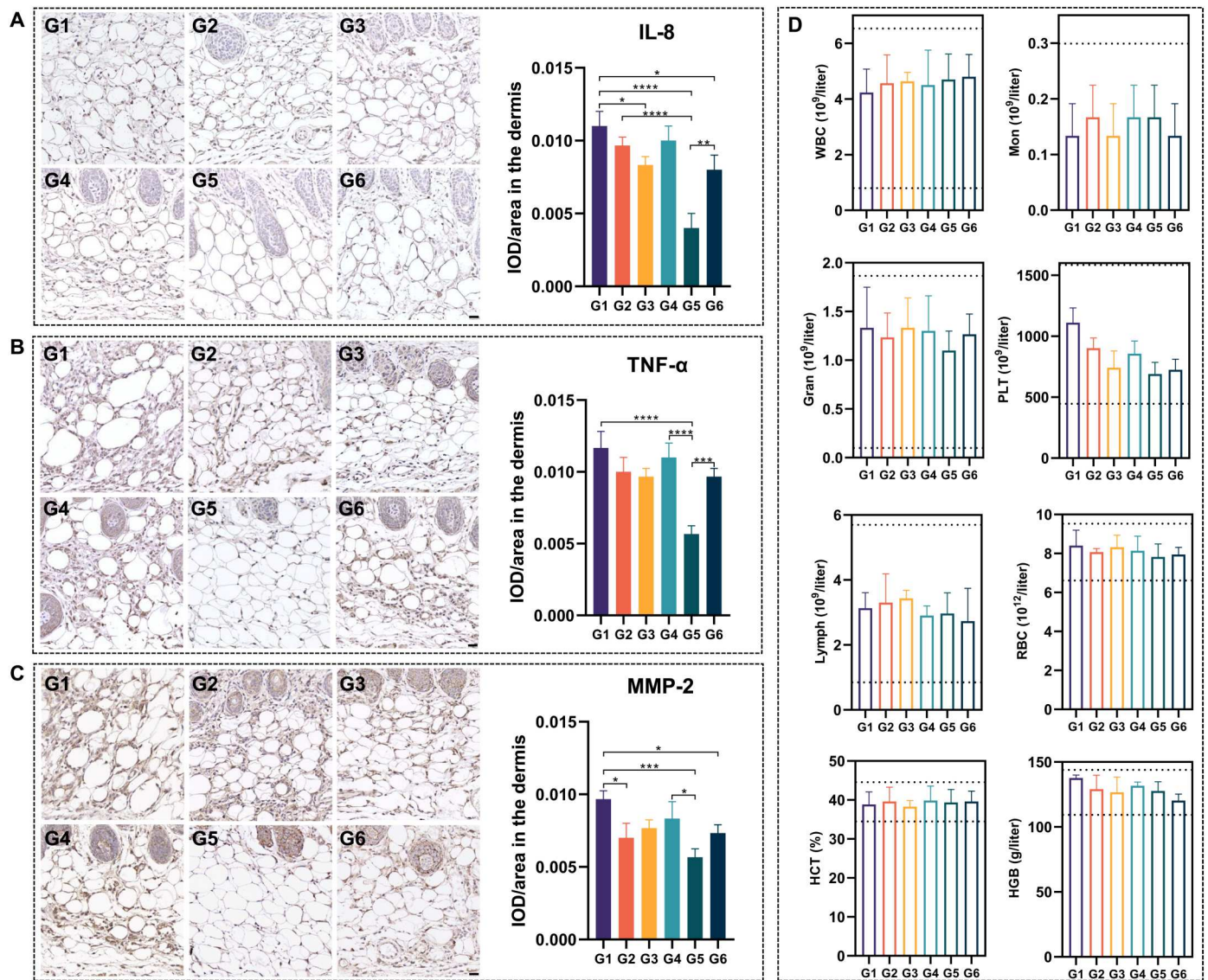


Fig. 8. Immunohistochemical analysis of acne after different treatments. (A) Representative images and optical density analysis of IL-8 protein expression in the tissue from acne area. (B) Representative images and optical density analysis of TNF- α protein expression in the tissue from acne area. (C) Representative images and optical density analysis of MMP-2 protein expression in the tissue from acne area. Scale bar (A–C), 20 μ m. IOD, integrated optical density. (D) Routine blood analysis from the day 7 mice. The range within the dotted line represents the normal norm. $n = 3$ independent experiments per group. Statistical differences were analyzed by one-way ANOVA and post hoc Tukey's test (* $P < 0.05$, ** $P < 0.01$, *** $P < 0.001$, and **** $P < 0.0001$). WBC, white blood cell count; Mon, monocyte; Gran, granulocyte; PLT, platelet count; Lymph, lymphocyte; RBC, red blood cell; HCT, hematocrit; HGB, hemoglobin.

responsive antibacterial nanomaterials to the MN patch that not only responds to bacterial infection quickly and efficiently but also are able to regulate the epidermal repair driven by fibroblasts.

In summary, we have developed a simple and effective approach to treat acne infection through the adoption of sonocatalytic antibacterial nanomaterials in MNs. The MNs made of biocompatible sodium hyaluronate can easily deliver ZnTCPP@ZnO to the acne lesion. The interfacial effect between ZnTCPP and ZnO within the composite structure has improved the electron transfer efficiency generated by ultrasound, thereby increasing the interfacial charge transfer to the adsorbed O_2 . In addition, the composite material reduces the activation energy of O_2 , and hence, a substantial

amount of 1O_2 can be produced under ultrasound irradiation that warrants the sonocatalytic antibacterial ability of the composite. In addition to the elimination of *P. acnes*, ZnTCPP@ZnO is able to intercept the infection induced by MRSA. The up-regulation of IL-8, TNF- α , and MMP-2 proteins expressed by the fibroblasts demonstrated that the system can effectively convince the skin tissue repair, when zinc ion release concurrently happens. The cytomic data suggested that two up-regulated genes, namely, *Mt1* and *Mt2*, were highly relevant to the absorption of zinc ions in the cells. Furthermore, the following up-regulated genes, i.e., *Rfc4*, *Rfc3*, *Lig1*, *Mcm6*, *Dut*, and *Dctcp1*, were evidenced in the process of DNA replication and the promotion of fibroblastic proliferation, suggesting that

these outcomes favored skin tissue repair. Last, we believe that the design of ultrasound driven MN patch not only can apply to treat acne infection efficiently but also may expand to other skin wound infections.

MATERIALS AND METHODS

Preparation of ZnTCPP@ZnO and MNs

To prepare the ZnTCPP@ZnO, 10.0 mg of 4,4,4,4-(porphine-5,10,15,20-tetrayl) tetrakis (benzoic acid) (TCPP) was dissolved in 50 ml of *N,N'*-dimethylformamide to form a homogeneous solution. After the addition of 10 ml of zinc nitrate (2.5 mg ml⁻¹; aqueous solution) and 10 mg of benzoic acid, the mixture was heated to 150°C and reacted for 80 min under stirring. Then, the ZnTCPP@ZnO was obtained by centrifugation and washed with ethanol several times. We used a freeze dryer to get ZnTCPP@ZnO powder for later use.

For the MNs, we dissolved 600 mg of sodium hyaluronate in 4 ml of deionized water and stirred it until completely dissolved. We then dropped 150 µl of solution onto the MN mold. After filling the mold, it was kept in a vacuum drying oven for 5 min. Bubbles in the mold were removed, and the mold was dried at room temperature for 12 hours to obtain the MN. To load the MNs with ZnTCPP@ZnO, the prepared nanoparticles were mixed into the dissolved sodium hyaluronate in the first step of patch fabrication before repeating the subsequent steps described above.

Characterization of nanoparticles and MNs

The microstructure of all samples was observed by FESEM (JSM6510LV and Zeiss Sigma 500), inverted fluorescence microscope (IFM; Olympus, IX73), and HRTEM (Tecnai G2 20 U-Twin and Titan G2 60-300). The mechanical properties of MNs were evaluated by a universal mechanical testing machine (Instron 5982). The surface chemical composition of the samples was analyzed using XPS (ESCALAB 250Xi, Thermo Fisher Scientific, USA). To determine the phase structure of the hydrogels, the samples were assessed by XRD (D8A25, Bruker, Germany) with a 2θ range from 20° to 80° and a step size of 0.02°. The PL spectra of the samples were measured using a fluorescence spectrophotometer (PerkinElmer LS55, USA). The sonocurrent and electrochemical impedance results were detected at an electrochemical workstation (CHI660E, China). Measurements of ROS were performed on ESR (Bruker EMXplus). The release of Zn²⁺ was recorded via inductively coupled plasma atomic emission spectrometry (Optimal 8000, PerkinElmer).

Theoretical calculations

We used the VASP to perform all the DFT calculations within the generalized gradient approximation using the Perdew–Burke–Ernzerhof formulation. The projected augmented wave potentials were chosen to describe the ionic cores and to take valence electrons into account using a plane wave basis set with a kinetic energy cutoff of 400 eV (50, 51). Partial occupancies of the Kohn-Sham orbitals were allowed using the Gaussian smearing method and a width of 0.05 eV (50, 51). Geometry optimization was considered convergent when the force change was smaller than 0.02 eV/Å. Grimme's DFT-D3 methodology was used to describe the dispersion interactions. In model 1, an MOF unit resides in a periodic box with side lengths of 25 Å by 25 Å by 20 Å. In model 2, one Zn (001) slab with two

Zn–O layers (81 Zn and 81 O atoms) was added to model 1. During structural optimizations, the Γ point in the Brillouin zone was used for *k*-point sampling, and all atoms were allowed to relax. Last, the transition states for the elementary reaction steps were determined by a combination of the nudged elastic band (NEB) method and the dimer method. In the NEB method, the path between the reactant and the product was discretized into a series of structural images (50, 51). The image closest to a likely transition state structure was then selected as an initial guess structure for the dimer method.

In vitro antibacterial activity assay

The spread plate method was used to analyze the antibacterial rate of all samples. *P. acnes* (CCTCC AB 2011019) suspensions (10⁵ CFUs/ml) were treated by diverse groups, including the control. The ultrasound parameter was set as 1.0 MHz, 1.5 W cm⁻², and 50% duty cycle for 15 min. After treatments, the diluted bacterial suspensions (20 µl) were collected and spread on Luria-Bertani agar plates and placed in a vacuum environment at 37°C for 2 days. Similarly, the MRSA (CCTCC AB 2015108) strain (10⁷ CFU/ml) was subjected to the same operation, except that MRSA only needed to be incubated at 37°C for 1 day. The morphologies of the treated bacteria were observed using FESEM. Further details of the procedure for the spread plate method and the formula for antibacterial efficacy can be found in our previous work (44).

In vitro cytotoxicity studies and cell-related experiments

NIH3T3 cells (RRID: CVCL_M025) were cultured in a medium supplemented with 10% fetal bovine serum and 1% penicillin-streptomycin solution (HyClone) in a humidified atmosphere of 5% CO₂ at 37°C, and the medium was changed every 2 days. Cell cytotoxicity was measured using the MTT assay. Before the MTT assay, all samples were prepared in 48-well plates. The cells were seeded onto the MNs in the 48-well plates. After culturing for 1, 3, and 7 days, 400 µl of MTT solution (5 µg/ml) was added to each well, and the cells were incubated at 37°C for 4 hours. After the medium was removed, 400 µl of dimethyl sulfoxide was added to each well, and the plates were shaken for 15 min on a shaking table. The supernatant fluid was assessed using a SpectraMax i3 platform (Molecular Devices, CA, USA). To align with the antimicrobial experimental protocol, all the MN samples used in the in vitro cell experiments were also exposed to ultrasound stimulation (1.0 MHz, 1.5 W cm⁻², and 50% duty cycle) for 15 min on the day 1 of cell culture and the culture continued until day 7. The cell viability was assessed on days 1, 3, and 7 by MTT assay. At day 1, the cells were washed thrice with PBS (pH 7.4), fixed in 4% formaldehyde solution for 10 min at room temperature, and rinsed thoroughly with PBS. Afterward, the samples were stained with fluorescein isothiocyanate–phalloidin (YiSen, Shanghai) at room temperature in darkness for 30 min and further stained with 4',6-diamidino-2-phenylindole (YiSen, Shanghai) for 30 s in darkness. The cell morphology of different samples was examined using an IFM (Olympus, IX73). For the transcriptome sequencing test and qRT-PCR analysis, 2 ml of NIH3T3 cell suspensions (1 × 10⁵ cells/ml) was cultured in six-well plates with different samples for 72 hours. The cell lysates were then stored at –80°C before sequencing using a triazolo reagent (Beyotime Biotechnology). RNA sequencing was performed using Illumina HiSeq X10 (Illumina, USA). The value of the gene expression was converted to log₁₀ (transcript per million readings + 1). The data were analyzed by the online Majorbio cloud platform. The

qRT-PCR primer sequences are listed in table S2. For the ELISA assay, the concentrations of cytokines in cell growth medium and cells were measured by an ELISA assay kit (Shanghai Jianglai Biotechnology Co. Ltd., Shanghai Enzyme-linked Biotechnology Co. Ltd.).

In vivo anti-acne experiments

The animal experimental process was approved by the Center for Food and Drug Safety Evaluation, Hubei Center for Disease Control and Prevention, Hubei Academy of Preventive Medicine. The animal experiment ethics approval number was 202110166. All animals were maintained and used in accordance with the Animal Management Rules of the Ministry of Health of the People's Republic of China and the *Guide for the Care and Use of Laboratory Animals—Chinese Version*. In addition, all animal experiments were conducted with the assistance of the Wuhan Pinuofei Biological Technology Co. Ltd.

Hemolysis assay test was conducted before the in vivo experiment. Fresh RBCs (4 ml) were separated by centrifuge at 3000 rpm for 10 min at 4°C, washed with saline for three times, and diluted to final concentration [5% (v/v)]. Different samples were separately added to 500 µl of RBCs and incubated at 37°C for 4 hours. At the end of incubation, the solution was centrifuged at 3000 rpm for 10 min at 4°C, and the hemolytic activity was determined at 570 nm with a microplate reader: Rate of hemolysis (%) = $[(OD_{\text{sample}} - OD_{\text{negative}})/(OD_{\text{positive}} - OD_{\text{negative}})] \times 100\%$.

The mice (Balb/c, female, 8 to 10 weeks, and 25 to 30 g) were weighed and anesthetized with the anesthetic isoflurane, the hair on the back of the mice was removed in a sterile biosafety cabinet using a shaving machine and a hair removal cream, and 100 µl of *P. acnes* (2×10^5 CFUs/ml) was intradermally injected into the skin of the back of the mice after disinfection of the skin with 75% alcohol cotton balls to establish an animal model of common acne. There were five mice per group. The mice were treated with different materials for 7 days. MNs were pressed into the skin by hand against the acne site and held for 3 min. The blank control group, medical acne ointment, patch, blank MN patch, MN patch, and MN patch were treated for 10 min with ultrasound (medical ultrasound probe, 1 cm in diameter). During the treatment period, the swelling volume of acne was measured daily with microcalipers. The changes in the acne on the back of mice were photographed and recorded at 1, 3, and 7 days after the experiment, and after euthanasia treatment, and the skin was cut along 2 mm of the wound edge to complete the tissue acquisition. The expression of factors related to wounds, underlying muscle repair, and inflammatory indexes were analyzed. For skin tissue acquisition and embedding tissue fixation, tissue fixation, tissue dehydration, tissue permeabilization, tissue wax immersion, tissue embedding, tissue sectioning were performed.

Statistical analysis

All data in this work are presented as mean values \pm SD. A one-way analysis of variance (ANOVA) and Student's *t* test were used for significance analysis. **P* < 0.05, ***P* < 0.01, ****P* < 0.001, and *****P* < 0.0001 were considered statistically significant. All experiments were repeated independently more than three times.

Supplementary Materials

This PDF file includes:

Figs. S1 to S10
Tables S1 and S2

[View/request a protocol for this paper from Bio-protocol.](#)

REFERENCES AND NOTES

1. A. M. O'Neill, M. C. Liggins, J. S. Seidman, T. H. Do, F. Li, K. J. Cavagnero, T. Dokoshi, J. Y. Cheng, F. Shafiq, T. R. Hata, J. E. Gudjonsson, R. L. Modlin, R. L. Gallo, Antimicrobial production by perifollicular dermal preadipocytes is essential to the pathophysiology of acne. *Sci. Transl. Med.* **14**, eabh1478 (2022).
2. B. Dreno, S. Pecastaings, S. Corvec, S. Veraldi, A. Khammari, C. Roques, Cutibacterium acnes (*Propionibacterium acnes*) and acne vulgaris: A brief look at the latest updates. *J. Eur. Acad. Dermatol. Venereol.* **32**, 5–14 (2018).
3. B. Dreno, What is new in the pathophysiology of acne, an overview. *J. Eur. Acad. Dermatol. Venereol.* **31**, 8–12 (2017).
4. T. Zhang, B. Sun, J. Guo, M. Wang, H. Cui, H. Mao, B. Wang, F. Yan, Active pharmaceutical ingredient poly(ionic liquid)-based microneedles for the treatment of skin acne infection. *Acta Biomater.* **115**, 136–147 (2020).
5. T. Waghule, G. Singhvi, S. K. Dubey, M. M. Pandey, G. Gupta, M. Singh, K. Dua, Microneedles: A smart approach and increasing potential for transdermal drug delivery system. *Biomed. Pharmacother.* **109**, 1249–1258 (2019).
6. A. Kar, N. Ahamad, M. Dewani, L. Awasthi, R. Patil, R. Banerjee, Wearable and implantable devices for drug delivery: Applications and challenges. *Biomaterials* **283**, 121435 (2022).
7. A. Liu, Q. Wang, Z. Zhao, R. Wu, M. Wang, J. Li, K. Sun, Z. Sun, Z. Lv, J. Xu, H. Jiang, M. Wan, D. Shi, C. Mao, Nitric oxide nanomotor driving exosomes-loaded microneedles for Achilles tendinopathy Healing. *ACS Nano* **15**, 13339–13350 (2021).
8. R. Jamaledin, C. K. Y. Yiu, E. N. Zare, L. N. Niu, R. Vecchione, G. Chen, Z. Gu, F. R. Tay, P. Makvandi, Advances in antimicrobial microneedle patches for combating infections. *Adv. Mater.* **32**, e2002129 (2020).
9. S. Li, D. Xia, M. R. Prausnitz, Efficient drug delivery into skin using a biphasic dissolvable microneedle patch with water-insoluble backing. *Adv. Funct. Mater.* **31**, 2103359 (2021).
10. Z. Chen, H. Li, Y. Bian, Z. Wang, G. Chen, X. Zhang, Y. Miao, D. Wen, J. Wang, G. Wan, Y. Zeng, P. Abdou, J. Fang, S. Li, C. J. Sun, Z. Gu, Bioorthogonal catalytic patch. *Nat. Nanotechnol.* **16**, 933–941 (2021).
11. M. Rademaker, Adverse effects of isotretinoin: A retrospective review of 1743 patients started on isotretinoin. *Australas. J. Dermatol.* **51**, 248–253 (2010).
12. J. S. Wang, Y. J. Hung, Y. C. Lu, C. L. Tsai, W. S. Yang, T. I. Lee, Y. C. Hsiao, W. H. Sheu, Difference between observed and predicted glycated hemoglobin at baseline and treatment response to vildagliptin-based dual oral therapy in patients with type 2 diabetes. *Diabetes Res. Clin. Pract.* **138**, 119–127 (2018).
13. Y. Qiu, G. Qin, S. Zhang, Y. Wu, B. Xu, Y. Gao, Novel lyophilized hydrogel patches for convenient and effective administration of microneedle-mediated insulin delivery. *Int. J. Pharm.* **437**, 51–56 (2012).
14. W. Park, V. P. Nguyen, Y. Jeon, B. Kim, Y. Li, J. Yi, H. Kim, J. W. Leem, Y. L. Kim, D. R. Kim, Y. M. Paulus, C. H. Lee, Biodegradable silicon nanoneedles for ocular drug delivery. *Sci. Adv.* **8**, eabn1772 (2022).
15. Y. Sun, J. Liu, H. Wang, S. Li, X. Pan, B. Xu, H. Yang, Q. Wu, W. Li, X. Su, Z. Huang, X. Guo, H. Liu, NIR laser-triggered microneedle-based liquid band-aid for wound care. *Adv. Funct. Mater.* **31**, 2100218 (2021).
16. N. G. Roupheal, M. Paine, R. Mosley, S. Henry, D. V. McAllister, H. Kalluri, W. Pewin, P. M. Frew, T. Yu, N. J. Thornburg, S. Kabbani, L. Lai, E. V. Vassilieva, I. Skountzou, R. W. Compans, M. J. Mulligan, M. R. Prausnitz, TIV-MNP 2015 Study Group, The safety, immunogenicity, and acceptability of inactivated influenza vaccine delivered by microneedle patch (TIV-MNP 2015): A randomised, partly blinded, placebo-controlled, phase 1 trial. *Lancet* **390**, 649–658 (2017).
17. Y. Liu, Y. Wang, W. Zhen, Y. Wang, S. Zhang, Y. Zhao, S. Song, Z. Wu, H. Zhang, Defect modified zinc oxide with augmenting sonodynamic reactive oxygen species generation. *Biomaterials* **251**, 120075 (2020).
18. Y. Yu, L. Tan, Z. Li, X. Liu, Y. Zheng, X. Feng, Y. Liang, Z. Cui, S. Zhu, S. Wu, Single-atom catalysis for efficient sonodynamic therapy of methicillin-resistant staphylococcus aureus-infected osteomyelitis. *ACS Nano* **15**, 10628–10639 (2021).
19. M. L. Guzman, R. M. Rossi, L. Karnischky, X. Li, D. R. Peterson, D. S. Howard, C. T. Jordan, The sesquiterpene lactone parthenolide induces apoptosis of human acute myelogenous leukemia stem and progenitor cells. *Blood* **105**, 4163–4169 (2005).

20. P. Huang, X. Qian, Y. Chen, L. Yu, H. Lin, L. Wang, Y. Zhu, J. Shi, Metalloporphyrin-encapsulated biodegradable nanosystems for highly efficient magnetic resonance imaging-guided sonodynamic cancer therapy. *J. Am. Chem. Soc.* **139**, 1275–1284 (2017).
21. Y. Luo, B. Li, X. Liu, Y. Zheng, E. Wang, Z. Li, Z. Cui, Y. Liang, S. Zhu, S. Wu, Simultaneously enhancing the photocatalytic and photothermal effect of NH₂-MIL-125-GO-Pt ternary heterojunction for rapid therapy of bacteria-infected wounds. *Bioact. Mater.* **18**, 421–432 (2022).
22. C. Mao, W. Zhu, Y. Xiang, Y. Zhu, J. Shen, X. Liu, S. Wu, K. M. C. Cheung, K. W. K. Yeung, Enhanced near-infrared photocatalytic eradication of MRSA biofilms and osseointegration using oxide perovskite-based P-N heterojunction. *Adv. Sci. (Weinh)* **8**, e2002211 (2021).
23. Y. Yu, Y. Cheng, L. Tan, X. Liu, Z. Li, Y. Zheng, T. Wu, Y. Liang, Z. Cui, S. Zhu, S. Wu, Theory-screened MOF-based single-atom catalysts for facile and effective therapy of biofilm-induced periodontitis. *Chem. Eng. J.* **431**, 133279 (2022).
24. J. Li, S. Song, J. Meng, L. Tan, X. Liu, Y. Zheng, Z. Li, K. W. K. Yeung, Z. Cui, Y. Liang, S. Zhu, X. Zhang, S. Wu, 2D MOF periodontitis photodynamic ion therapy. *J. Am. Chem. Soc.* **143**, 15427–15439 (2021).
25. A. B. Lansdown, U. Mirastschijski, N. Stubbs, E. Scanlon, M. S. Agren, Zinc in wound healing: Theoretical, experimental, and clinical aspects. *Wound Repair Regen.* **15**, 2–16 (2007).
26. A. R. Lemans, E. Noguchi, The replication fork: Understanding the eukaryotic replication machinery and the challenges to genome duplication. *Genes (Basel)* **4**, 1–32 (2013).
27. N. Chiarelli, G. Carini, N. Zoppi, M. Ritelli, M. Colombi, Molecular insights in the pathogenesis of classical Ehlers-Danlos syndrome from transcriptome-wide expression profiling of patients' skin fibroblasts. *PLoS One* **14**, e0211647 (2019).
28. A. Droit, J. M. Hunter, M. Rouleau, C. Ethier, A. Picard-Cloutier, D. Bourgeois, G. G. Poirier, PARPs database: A LIMS systems for protein-protein interaction data mining or laboratory information management system. *BMC Bioinformatics* **8**, 483 (2007).
29. J. A. Burdick, G. D. Prestwich, Hyaluronic acid hydrogels for biomedical applications. *Adv. Mater.* **23**, H41–H56 (2011).
30. P. Makvandi, R. Jamaledin, G. Chen, Z. Baghbantarghadari, E. N. Zare, C. Di Natale, V. Onesto, R. Vecchione, J. Lee, F. R. Tay, P. Netti, V. Mattoli, A. Jaklenc, Z. Gu, R. Langer, Stimuli-responsive transdermal microneedle patches. *Mater. Today (Kidlington)* **47**, 206–222 (2021).
31. M. Niazi, E. Alizadeh, A. Zarebkohan, K. Seidi, M. H. Ayoubi-Joshaghani, M. Azizi, H. Dadashi, H. Mahmudi, T. Javaheri, M. Jaymand, M. R. Hamblin, R. Jahanban-Esfahlan, Z. Amoozgar, Advanced bioresponsive multitasking hydrogels in the new era of biomedicine. *Adv. Funct. Mater.* **31**, 2104123 (2021).
32. J. H. Park, M. G. Allen, M. R. Prausnitz, Biodegradable polymer microneedles: Fabrication, mechanics and transdermal drug delivery. *J. Control. Release* **104**, 51–66 (2005).
33. A. H. Sabri, Y. Kim, M. Marlow, D. J. Scurr, J. Segal, A. K. Banga, L. Kagan, J. B. Lee, Intradermal and transdermal drug delivery using microneedles - Fabrication, performance evaluation and application to lymphatic delivery. *Adv. Drug Deliv. Rev.* **153**, 195–215 (2020).
34. Y. Zhao, L. Jiang, L. Shangguan, L. Mi, A. Liu, S. Liu, Synthesis of porphyrin-based two-dimensional metal-organic framework nanodisk with small size and few layers. *J. Mater. Chem. A* **6**, 2828–2833 (2018).
35. L. Hang, T. Zhang, H. Wen, L. Liang, W. Li, X. Ma, G. Jiang, Controllable photodynamic performance via an acidic microenvironment based on two-dimensional metal-organic frameworks for photodynamic therapy. *Nano Research* **14**, 660–666 (2021).
36. C. Cheng, A. Amini, C. Zhu, Z. Xu, H. Song, N. Wang, Enhanced photocatalytic performance of TiO₂-ZnO hybrid nanostructures. *Sci. Rep.* **4**, 4181 (2014).
37. J. Li, X. Liu, L. Tan, Y. Liang, Z. Cui, X. Yang, S. Zhu, Z. Li, Y. Zheng, K. W. K. Yeung, X. Wang, S. Wu, Light-activated rapid disinfection by accelerated charge transfer in red phosphorus/ZnO heterointerface. *Small Methods* **3**, 1900048 (2019).
38. W. R. Cai, H. B. Zeng, H. G. Xue, R. S. Marks, S. Cosnier, X. J. Zhang, D. Shan, Enhanced electrochemiluminescence of porphyrin-based metal-organic frameworks controlled via coordination modulation. *Anal. Chem.* **92**, 1916–1924 (2020).
39. Y. P. Wei, Y. W. Zhang, J. S. Chen, C. J. Mao, B. K. Jin, An electrochemiluminescence biosensor for p53 antibody based on Zn-MOF/GO nanocomposite and Ag(+)-DNA amplification. *Mikrochim. Acta* **187**, 455 (2020).
40. P. Sehgal, A. K. Narula, Metal substituted metalloporphyrins as efficient photosensitizers for enhanced solar energy conversion. *J. Photochem. Photobiol. A Chem.* **375**, 91–99 (2019).
41. H. T. Vo, A. T. Nguyen, C. V. Tran, S. X. Nguyen, N. T. Tung, D. T. Pham, D. D. Nguyen, D. D. La, Self-assembly of porphyrin nanofibers on ZnO nanoparticles for the enhanced photocatalytic performance for organic dye degradation. *ACS Omega* **6**, 23203–23210 (2021).
42. J. Jing, J. Yang, Z. Zhang, Y. Zhu, Supramolecular zinc porphyrin photocatalyst with strong reduction ability and robust built-in electric field for highly efficient hydrogen production. *Adv. Energy Mater.* **11**, 2101392 (2021).
43. Y. Li, X. Liu, L. Tan, Z. Cui, X. Yang, Y. Zheng, K. W. K. Yeung, P. K. Chu, S. Wu, Rapid sterilization and accelerated wound healing using Zn²⁺ and graphene oxide modified g-C₃N₄ under dual light irradiation. *Adv. Funct. Mater.* **28**, 1800299 (2018).
44. Y. Xiang, C. Mao, X. Liu, Z. Cui, D. Jing, X. Yang, Y. Liang, Z. Li, S. Zhu, Y. Zheng, K. W. K. Yeung, D. Zheng, X. Wang, S. Wu, Rapid and superior bacteria killing of carbon quantum dots/ZnO decorated injectable folic acid-conjugated PDA hydrogel through dual-light triggered ROS and membrane permeability. *Small* **15**, e1900322 (2019).
45. M. Zhao, Y. Wang, Q. Ma, Y. Huang, X. Zhang, J. Ping, Z. Zhang, Q. Lu, Y. Yu, H. Xu, Y. Zhao, H. Zhang, Ultrathin 2D Metal-Organic Framework Nanosheets. *Adv. Mater.* **27**, 7372–7378 (2015).
46. Y.-Z. Chen, Z. U. Wang, H. Wang, J. Lu, S.-H. Yu, H.-L. Jiang, Singlet oxygen-engaged selective photo-oxidation over Pt nanocrystals/porphyrinic MOF: The roles of photothermal effect and Pt electronic state. *J. Am. Chem. Soc.* **139**, 2035–2044 (2017).
47. Y. Harada, K. Ogawa, Y. Irie, H. Endo, L. B. Feril Jr., T. Uemura, K. Tachibana, Ultrasound activation of TiO₂ in melanoma tumors. *J. Control. Release* **149**, 190–195 (2011).
48. L. Tan, Z. Zhou, X. Liu, J. Li, Y. Zheng, Z. Cui, X. Yang, Y. Liang, Z. Li, X. Feng, S. Zhu, K. W. K. Yeung, C. Yang, X. Wang, S. Wu, Overcoming multidrug-resistant MRSA using conventional aminoglycoside antibiotics. *Adv. Sci. (Weinh)* **7**, 1902070 (2020).
49. X. Feng, J. Lei, L. Ma, Q. Ouyang, Y. Zeng, H. Liang, C. Lei, G. Li, L. Tan, X. Liu, C. Yang, Ultrasonic interfacial engineering of MOS₂-modified Zn single-atom catalysts for efficient osteomyelitis sonodynamic ion therapy. *Small* **18**, e2105775 (2022).
50. G. Kresse, J. Furthmüller, Efficient iterative schemes for ab initio total-energy calculations using a plane-wave basis set. *Physical Rev. B. Condens. Matter.* **54**, 11169–11186 (1996).
51. G. Kresse, J. Furthmüller, Efficiency of ab-initio total energy calculations for metals and semiconductors using a plane-wave basis set. *Comput. Mater. Sci.* **6**, 15–50 (1996).
52. Y. Nosaka, A. Y. Nosaka, Generation and detection of reactive oxygen species in photocatalysis. *Chem. Rev.* **117**, 11302–11336 (2017).
53. X. Shen, W. Liu, X. Gao, Z. Lu, X. Wu, X. Gao, Mechanisms of oxidase and superoxide dismutation-like activities of gold, silver, platinum, and palladium, and their alloys: A general way to the activation of molecular oxygen. *J. Am. Chem. Soc.* **137**, 15882–15891 (2015).
54. J. Li, L. Tan, X. Liu, Z. Cui, X. Yang, K. W. K. Yeung, P. K. Chu, S. Wu, Balancing bacteria-osteoblast competition through selective physical puncture and biofunctionalization of ZnO/polydopamine/arginine-glycine-aspartic acid-cysteine nanorods. *ACS Nano* **11**, 11250–11263 (2017).
55. M. Yin, J. Wu, M. Deng, P. Wang, G. Ji, M. Wang, C. Zhou, N. T. Blum, W. Zhang, H. Shi, N. Jia, X. Wang, P. Huang, Multifunctional magnesium organic framework-based microneedle patch for accelerating diabetic wound healing. *ACS Nano* **15**, 17842–17853 (2021).
56. F. F. Song, L. L. Xia, P. Ji, Y. B. Tang, Z. M. Huang, L. Zhu, J. Zhang, J. Q. Wang, G. P. Zhao, H. L. Ge, Y. Zhang, Y. Wang, Human dCTP pyrophosphatase 1 promotes breast cancer cell growth and stemness through the modulation on 5-methyl-dCTP metabolism and global hypomethylation. *Oncogenesis* **4**, e159 (2015).
57. J. L. Huffman, H. Li, R. H. White, J. A. Tainer, Structural basis for recognition and catalysis by the bifunctional dCTP deaminase and dUTPase from *Methanococcus jannaschii*. *J. Mol. Biol.* **331**, 885–896 (2003).
58. Y. Zhang, P. Feng, J. Yu, J. Yang, J. Zhao, J. Wang, Q. Shen, Z. Gu, ROS-responsive microneedle patch for acne vulgaris treatment. *Adv. Ther.* **1**, 1800035 (2018).
59. Y. B. Lee, E. J. Byun, H. S. Kim, Potential role of the microbiome in acne: A comprehensive review. *J. Clin. Med.* **8**, 987 (2019).

Acknowledgments: We thank all our partners for efforts and help. **Funding:** This work was jointly supported by the National Key R&D Program of China (2018YFA0703100), the General Research Fund of Hong Kong Research Grant Council (nos. 17207719 and 17214516), the Hong Kong Health and Medical Research Fund (nos.19180712, 20190422, and 21200592), the Innovation and Technology Fund Partnership Research Program (PRP/030/30FX), the National Science Fund for Distinguished Youth Scholar (no. 51925104), Shenzhen Science and Technology Funding (nos. JSGG20180507183242702 and JCYJ20210324120009026), and the Sanming Project of Medicine in Shenzhen "Team of Excellence in Spinal Deformities and Spinal Degeneration" (SZSM201612055). **Author contributions:** Y.X., S.W., and K.W.K.Y. conceived and designed the concept of the experiments. Y.X. synthesized the materials and conducted the material characterizations. Y.X., C.M., Y.Z., C.W., and J.L. analyzed the experimental data and cowrote the manuscript. X.L., J.W., K.Y.H.K., K.M.C.C., S.W., and K.W.K.Y. provided important experimental insights. All the authors discussed, commented on, and agreed on the manuscript. **Competing interests:** The authors declare that they have no competing interests. **Data and materials availability:** All data needed to evaluate the conclusions in the paper are present in the paper and/or the Supplementary Materials.

Submitted 29 September 2022

Accepted 3 February 2023

Published 8 March 2023

10.1126/sciadv.adf0854